Reconstruction of the Rheological Parameters in a Sea Ice Model with Viscoplastic Rheology

GLEB PANTELEEV,[a] MAX YAREMCHUK,[a] AND OCEANA FRANCIS[b]

[a] *Naval Research Laboratory, Stennis Space Center, Mississippi*
[b] *University of Hawai'i at Mānoa, Honolulu, Hawaii*

(Manuscript received 26 October 2021, in final form 16 August 2022)

ABSTRACT: We analyzed the feasibility of the reconstruction of the spatially varying rheological parameters through the four-dimensional variational data assimilation of the sea ice velocity, thickness, and concentration into the viscoplastic (VP) sea ice model. The feasibility is assessed via idealized variational data assimilation experiments with synthetic observations configured for a 1-day data assimilation window in a 50 × 40 rectangular basin forced by the open boundaries, winds, and ocean currents and should be viewed as a first step in the developing the similar algorithms which can be applied for the more advanced sea ice models. It is found that "true" spatial variability (~5.8 kN m^{-2}) of the internal maximum ice strength parameter P^* can be retrieved from observations with reasonable accuracy of 2.3–5.3 kN m^{-2}, when an observation of the sea ice state is available daily in each grid point. Similar relative accuracy was achieved for the reconstruction of the compactness strength parameter α. The yield curve eccentricity e is found to be controlled by the data with less efficiency, but the spatial mean value of e could be still reconstructed with a similar degree of confidence. The accuracy of P^*, α, and e retrievals is found to increase in regions of stronger ice velocity convergence, providing prospects for better processing of the observations collected during the recent MOSAiC experiment. The accuracy of the retrievals strongly depends on the number of the control variables characterizing the rheological parameter fields.

KEYWORDS: Ocean dynamics; Inverse methods; Data assimilation

1. Introduction

Sea ice models are important components of environmental modeling at high latitudes utilized for climate studies on different time scales. In modern formulations, the sea ice cover is often represented as a two-dimensional granular sea ice floe field covering the ocean surface and forced by winds and ocean currents. During the last decade, there were multiple efforts to apply such a discrete element approach for the high-resolution modeling of the sea ice (e.g., Hopkins et al. 2004; Hopkins and Thorndike 2006; Herman 2016). However, due to the relatively large computational cost of discrete element sea ice models, the continuum models remain in the mainstream of sea ice modeling tools with a wide range of temporal and spatial scales. Many of these models (e.g., Heimbach et al. 2010; Zhang and Rothrock 2003; Vancoppenolle et al. 2009; Kauker et al. 2009) are based on the viscoplastic (VP) rheology proposed by Hibler (1979), which requires a relatively expensive implicit solver for the momentum equation (Hibler 1979; Zhang and Hibler 1997; Lemieux et al. 2008, 2012; Losch et al. 2014). Another group of the sea ice models follow the elastic VP (EVP) rheology (Hunke and Dukowicz 1997). This approach was proposed as an alternative explicit method, which can be easily adopted for massive parallel supercomputer architectures and is, thus, rather efficient for high-resolution sea ice modeling (e.g., Hunke and Lipscomb 2010; Koldunov et al. 2019).

The common feature of the VP and EVP rheologies is their control from three parameters (P^*, e, and α), describing, respectively, the maximum ice strength (internal pressure) per unit thickness, the yield curve axes ratio, and the scaling of ice strength with its compactness. Throughout the manuscript we will use both compactness and concentration terms suggesting that they are similar and range between 0 and 1.

In most model settings, the above-mentioned rheological parameters (RPs) do vary in space and their values are defined empirically from multiple numerical experiments. RPs, such as P^* and e, reflect the model parameterization rather than physics and, thus, are directly unobservable (Kreyscher et al. 2000) but are, nevertheless, known with a certain range (Harder and Fischer 1999).

The typical values of P^* derived from sea ice velocity observations vary from 15 to 20 kN m^{-2} (Kreyscher et al. 1997) up to 30–45 kN m^{-2} (Tremblay and Hakakian 2006), while the standard value of P^* remains close to 27.5 kN m^{-2} (Hibler and Walsh 1982). This suggests the possibility of significant variability of P^*, which may be attributed to both nonphysical considerations (such as spatially variable model resolution), and spatiotemporal variations of the sea ice. There are multiple factors (e.g., sea ice salinity, temperature, and age; Anderson and Weeks 1958), which affect the physical properties of the sea ice which formally should result in different rheological properties of different sea ice categories.

Thus, it is reasonable to propose that the rheological parameters (e.g., P^* and e) are not constant but may vary in space and time. Multiple modeling experiments and sea ice observations (e.g., Juricke et al. 2013; Toyota and Kimura 2018) indicate that spatially varying and properly defined RPs should significantly improve the sea ice model performance. Juricke and Jung (2014) showed that stochastic (in space and time) sea ice strength parameterization may have a significant impact on the sea ice state in climatological models.

Corresponding author: Gleb Panteleev, gleb.panteleev@nrlssc.navy.mil

DOI: 10.1175/JTECH-D-21-0158.1

The early attempts of defining sea ice model parameters in an optimal way utilized a traditional "trial-and-error" approach, involving multiple runs of a sea ice model with different sets of RPs (e.g., Miller et al. 2006; Uotila et al. 2012). The recent more advanced methods are based on the Green's function approach (Nguyen et al. 2011), ensemble Kalman filtering (Massonnet et al. 2014), and genetic algorithms (Sumata et al. 2019).

Recently, Stroh et al. (2019) conducted a set of observing system simulation experiments (OSSEs) with a simple one-dimensional VP sea ice model and demonstrated that spatially varying RPs can be reconstructed from sea ice observations of velocity, thickness, and concentration using a standard variational data assimilation approach. In a 2D setting of the OSSEs with the EVP model, Panteleev et al. (2020) showed that spatially varying P^* and e can be reasonably well reconstructed at grid resolutions of 15–30 km through the variational data assimilation procedure.

Due to the instability of the EVP tangent linear/adjoint (TLA) models, Panteleev et al. (2020) utilized Newtonian dumping regularization and suggested that the implicit VP formulation with stable VP TL/ADJ models could be a more attractive option for RP retrievals from observations. It was also found that optimization of spatially varying RPs provided a significantly better short-range forecast but required improvement of the ice thickness observations accuracy by at least 2 times compared to those from the *CryoSat-2* satellite (Alexandrov et al. 2010; Laxon et al. 2013; Tilling et al. 2018). The accuracy of the existing sea ice velocity and concentration observations were found to be sufficient for optimization of the spatially varying RPs.

Insufficient accuracy of the ice thickness data currently imposes a limitation on the feasibility of applying the four-dimensional variational (4Dvar) data assimilation (DA) approach to the real observations. Meanwhile, in the course of the recent MOSAiC observational program (https://mosaic-expedition.org/) sea ice researchers obtained a set of very accurate sea ice, atmospheric and ocean observations in a limited region (~375 km × 280 km) where ice dynamics is strongly controlled by open boundary (OB) forcing (J. Hutchings 2022, personal communication). To explore the dynamically constrained inversions of the MOSAiC data, there is a need to show the feasibility of such an approach in a region dominated by the OB forcing at a relatively high (5–7 km) spatial resolution. Dominance of the OB control increases the dimension of the control space and inherently causes additional ill-posedness of the inversion algorithm (e.g., Bennet 1992), whereas higher spatial resolution inevitably brings in stronger nonlinearity effectively decreasing the DA window where the tangent linear approximation remains valid.

In this study, we extend the results of Panteleev et al. (2020) and analyze the feasibility of RP optimization within a more advanced 2D sea ice model based on the VP rheology formulation of Lemieux et al. (2008), which now includes open boundaries and more accurate formulation of the ocean currents and wind forcings.

Taking into account that land fast ice phenomenon is not observed in deep and open areas of the Arctic Ocean we focus on the retrieval of the RPs responsible for the sea ice rheology only (i.e., P^*, e, and α) and do not consider feasibility of optimizing the parameters responsible for Land Fast sea ice parameterization discussed by Panteleev et al. (2020). Our approach is similar to the one utilized in Panteleev et al. (2020), and follows the conventional twin-data (or OSSE) experimental approach (e.g., Goldberg and Heimbach 2013; Nitta 1975; Arnold and Dey 1986; Nichols 2003, 2010). The limitation of the OSSEs approach is that data are generated using the same sea ice model, while the real sea ice behavior is more complicated and should be described by a more complicated model which takes into the account floes interaction (e.g., Tremblay and Mysak 1997). Meanwhile, the OSSEs can be viewed as a natural initial test bed for any data assimilation model.

The paper is organized as follows: Section 2 describes the sea ice model and the details of constructed TLA codes. Section 3 provide details of the OSSEs and the procedure we used for the generation of synthetic observations and the first-guess solution. Results of the OSSE experiments are described in section 4, optimization of the compressive strength, yield curve axes ratio, and compactness strength parameter, with special focus on the feasibility of optimizing spatially varying RPs in the context of the MOSAiC observations, which should be publicly available in the near future. Section 5 summarizes the work and discusses directions of future research.

2. Sea ice model and its 4Dvar implementation

a. *Viscoplastic sea ice model*

1) Formulation

In the present study, we employed the sea ice model based on the formulation of Lemieux et al. (2008) with added basal stress parameterization Lemieux et al. (2015, 2016) and generalized Hibler (1979) yield curve. Equations of the model describe VP ice physics coupled with sea ice dynamics which is forced by the stresses $\boldsymbol{\tau}$ exerted on ice through its interaction with the bottom $\boldsymbol{\tau}_b$, atmosphere $\boldsymbol{\tau}_a$, and the ocean $\boldsymbol{\tau}_w$:

$$\rho h A(\partial_t + f\mathbf{k}\times)\mathbf{u} = \mathrm{div}\boldsymbol{\sigma} + \boldsymbol{\tau}_a + \boldsymbol{\tau}_w, \tag{1}$$

$$\partial_t h = \mathrm{div}\,(h\mathbf{u}), \tag{2}$$

$$\partial_t A = \mathrm{div}\,(A\mathbf{u}). \tag{3}$$

Here, $\mathbf{u} = \{u, v\}$, h, and A are the 2D fields of sea ice velocities, ice effective thickness, and concentration, div is the divergence operator; and $\mathbf{k}$ is the vertical unit vector. With a VP formulation (Hibler 1979), $\boldsymbol{\sigma}$ is the 2D field of ice stress tensor defined through the deformation rate tensor $\dot{\boldsymbol{\epsilon}}$:

$$\boldsymbol{\sigma} = \begin{vmatrix} \sigma_{xx} & \sigma_{xy} \\ \sigma_{xy} & \sigma_{yy} \end{vmatrix}, \ \sigma_{ij} = 2\eta\dot{\epsilon}_{ij} + \mathbf{E}[(\zeta - \eta)\mathrm{Tr}(\dot{\boldsymbol{\epsilon}}) - P/2], \tag{4}$$

$$\dot{\boldsymbol{\epsilon}} = \frac{1}{2}\begin{vmatrix} 2u_x & v_x + u_y \\ v_x + u_y & 2v_y \end{vmatrix}, \tag{5}$$

where $\mathbf{E}$ is the identity matrix and the pressure term P is parameterized as

TABLE 1. Model and assimilation system configuration parameters.

Name	Symbol	Value/range
Constant parameters		
Coriolis parameter	f	10^{-4} s^{-1}
Ice density	ρ	900 kg m^{-2}
Air density	ρ_a	1.3 kg m^{-3}
Water density	ρ_w	1026 kg m^{-3}
Air drag coefficient	C_a	0.001
Water drag coefficient	C_w	0.004
Air turning angle	θ_a	0.436 332 3 rad
Water turning angle	θ_w	0.436 332 3 rad
Time step	δt	2160 s
Creep limit	Δ^*	10^{-10} s^{-1}
Controlled parameter fields		
Base strength parameter	P^*	17.5–37.5 kN m^{-2}
Yield curve axes ratio	e	1.1–2.9
Compactness strength parameter	α	20 (25)

$$P = P^* hA \exp\,[-\alpha(1 - A)], \tag{6}$$

where P^* and α are, respectively, the ice compressive strength and the compactness strength parameter. The typical values of the ice strength P^* and α are listed in Table 1. According to Hibler (1979) and König Beatty and Holland (2010), ζ and η are the bulk and shear viscosities

$$\zeta = \frac{P}{2\Delta},\ \eta = \frac{\zeta}{e^2}, \tag{7}$$

$$\Delta(\dot{\epsilon}) = \frac{1}{e}[(e^2 - 1)(\mathrm{tr}\dot{\epsilon})^2 + 2\mathrm{tr}(\dot{\epsilon}^2)]^{-1/2}, \tag{8}$$

where e is the ratio of the axes of the elliptical yield curve and k_T is the empirical parameter controlling the tensile strength. To avoid numerical singularities at $\dot{\epsilon} = 0$, the values of $\Delta(\dot{\epsilon})$ are limited from below by the additional parameter $\Delta^* = 10^{-10}$, so that $\Delta(\dot{\epsilon}) = \max(\Delta^*, \Delta)$. The atmospheric, ocean, and bottom stresses in Eq. (1) were parameterized in accordance with Lemieux et al. (2015, 2016) and Hunke and Lipscomb (2010):

$$\boldsymbol{\tau}_a = -C_a \rho_a A |\mathbf{u}_a^g| \mathbf{R}_{\theta_a}(\mathbf{u}_a^g), \tag{9}$$

$$\boldsymbol{\tau}_w = -C_w \rho_w A |\mathbf{u} - \mathbf{u}_w| \mathbf{R}_{\theta_w}(\mathbf{u} - \mathbf{u}_w), \tag{10}$$

where θ is the Heaviside step function, $\mathbf{h}_b$ is the ocean depth, $\mathbf{R}_{\theta_a}$ and $\mathbf{R}_{\theta_w}$ are 2×2 matrices rotating the velocity vector by the turning angles θ_a and θ_w counterclockwise, and $\mathbf{u}_a^g$ and $\mathbf{u}_w$ are the atmospheric wind and water velocities, respectively. The values of other parameters C_a, C_w, ρ_a, and ρ_w are listed in Table 1. Similar to the recent study by Panteleev et al. (2020), we focus on the retrieval of the spatial variability of P^* and e from synthetic observations of the sea ice state in the 375 km $\times$ 280 km domain with horizontal resolutions of 7.5 and 7 km, respectively. The dimension of the model grid was 50 $\times$ 40 elements. The sea ice was forced by spatially and temporally varying wind, ocean currents, and sea ice inflow (or outflow) through the open boundaries.

2) NUMERICAL SCHEME

A conventional way to solve the nonlinear momentum Eq. (1) is to use the iterative procedure, where a sequence of K linear equations is solved

$$\mathbf{M}_k(\mathbf{X}^k)\mathbf{u}^{k+1} = \mathbf{b}_k(\mathbf{X}^k), \quad \mathbf{X}^k = (\mathbf{u}^k, h^k, A^k); \quad k = 1,\ldots,K \tag{11}$$

with respect to the unknown ice velocities $\mathbf{u}^{k+1}$ on the next $(k + 1)$th iteration while the elements of the system matrices $\mathbf{M}_k$ and the right-hand-side vectors $\mathbf{b}_k$ depend on the sea ice states $\mathbf{X}^k = (\mathbf{u}^k, h^k, A^k)$ at the previous (kth) iteration.

To solve Eqs. (11) we used the GMRES algorithm (Saad 2003) with incomplete LU factorization preconditioning. This approach follows the algorithm of Lemieux et al. (2008), but it is formulated on the B grid and utilizes the standard GMRES routine from the ITSOL package available at https://www-users.cse.umn.edu/~saad/index.html. It is necessary to note that the 4Dvar data assimilation technique requires storing the entire set of K arrays $\mathbf{M}_k$ and $\mathbf{b}_k$, which may be expensive if K is large. In our case, the number of equations in (12) was relatively small (3822) and we utilized $K = 10$ as suggested by Lemieux et al. (2008), and Lemieux and Dupont (2020).

b. *Variational DA with VP sea ice model*

1) STRONG CONSTRAINT FORMULATION

In the variational DA experiments, we used the strong constraint state-space formulation of the problem, which minimizes the cost function on the manifold $\mathbf{N}$, whose structure is specified by the model equations. The cost function J was defined by

$$\begin{aligned} J = 0.5\sum_{\Omega}[&W_h(h - h')^2 + W_A(A - A')^2 + W_u(u - u')^2 \\ &+ \tilde{W}_h(\hat{D}h^2) + \tilde{W}_A(\hat{D}A)^2 + \tilde{W}_u(\hat{D}u)^2 + \tilde{W}_p(\hat{D}P^*)^2 \\ &+ \tilde{W}_e(\hat{D}e)^2]. \end{aligned} \tag{12}$$

Here, W and $\tilde{W}$ denote nonzero elements of the diagonal inverse error covariance matrices of the fields in the parentheses, $\hat{D}$ is the Laplacian operator, simulated observations are denoted by primes, and summation is made over the entire space–time computational grid Ω. The first three terms attract the optimized solution to the data, while the rest penalize gridscale components of the optimized fields and tend to penalize gridscale components and enforce smoothness of the optimized fields.

To decrease the number of control variables at the open boundaries, atmospheric and oceanic forcing were specified at the beginning and at the end of the period of integration (~1 day) and linearly interpolated in-between. In addition, atmospheric wind, ocean currents, and sea surface height and all other model parameters were specified on the sparse

2D grid (in every tenth node of the computational grid) and then spatially interpolated on the model grid using the bilinear interpolation operator Ĭ.

To constrain the minimization process to the manifold defined by the finite difference analog of Eqs. (1)–(11), we define the vector of control variables $\mathbf{C} = [\mathbf{C}_0, \mathbf{C}_{\mathrm{OBC}}, \mathbf{C}_p]$, which includes 7822 variables elements of the initial state of the model $\mathbf{C}_0 \equiv \mathbf{X}|_{t=0}$ (i.e., initial sea ice velocity, thickness, and concentration), 1064 open boundary conditions $\mathbf{C}_{\mathrm{OBC}}$ and other control fields $\mathbf{C}_p$, which contain rheological parameters and atmospheric and oceanic forcing fields. Note that the vector of model trajectory $\mathbf{X}$ is a nonlinear function of the control vector $\mathbf{C}$, whose constituent $\mathbf{C}_{\mathrm{OBC}}$ was defined at the beginning and at the end of the period of integration, while constituent $\mathbf{C}_p$ was defined on a sparser 2D grid (in every tenth node of the computational grid) as described above. In the OSSEs described below, the size of the control vector did not exceed 8934 elements.

2) Adjoint and tangent linear models

Technically, apart from developing the sea ice model code, the minimization of the cost function J requires development of the routines for computing its gradients, as well as the tangent linear model $\mathbf{N}_X$ and its adjoint $\mathbf{N}_X^{\mathrm{T}}$. The machinery of deriving these codes is based on the rules of differentiation and was realized in multiple software packages (e.g., Giering and Kaminski 1998; http://autodiff.com/tamc), OpenAD (https://www.mcs.anl.gov/OpenAD; Goldberg and Heimbach 2013), but in our case, TLA were coded by hand. The tangent linear code was derived by analytic differentiation of the above-mentioned numerical scheme in the vicinity of a background model trajectory. The adjoint code was obtained by implicit transposition of the sparse matrix in the code simulating the action of the tangent linear operator $\mathbf{N}_X$ on the state vector perturbation $\delta\mathbf{X}$. More detailed description of the TLA codes for the sea ice model and the gradients with respect to the control variables can be found in Panteleev et al. (2020). The basic principles of the variational techniques of data assimilation in different geophysical applications can also be found in numerous publications (e.g., Penenko 1981; Le Dimet 1982; Lewis and Derber 1985; Le Dimet and Talagrand 1986; Wunsch 1996; Errico 1997).

The most laborious part in deriving the TLA model codes was linearization of Eqs. (11) with respect to ice velocities and RPs for each iteration cycle:

$$\mathbf{M}_k(\mathbf{X}^k)\delta\mathbf{u}^{k+1} = \delta\mathbf{u}^k\left[\frac{\delta\mathbf{M}_k}{\delta\mathbf{u}^k}\mathbf{u}^k + \frac{\delta\mathbf{b}_k}{\delta\mathbf{u}^k}\right], \quad k = 1, \ldots, K. \qquad (13)$$

Here $\mathbf{b}_{\mathbf{u}}(\mathbf{X})$ and $\mathbf{M}_{\mathbf{u}}$ denote derivatives of the elements of $\mathbf{b}$ and $\mathbf{M}$ with respect to ice velocity $\mathbf{u}$ in the vicinity of $\mathbf{X}^k$. Note that the left-hand side of (13) contains the same matrices $\mathbf{M}_k$ as the forward model (11). This property of the TLA guarantees solvability of Eq. (13) providing the sequence of solutions to the forward model (11), and allows the employment of $\mathbf{M}_k$ from the forward model run for use in the respective TLA models. Similar to the 1D VP sea ice model (Stroh et al. 2019), we found that the TLA of the 2D VP sea ice model is stable and does not require additional regularization (e.g., Hoteit et al. 2005; Panteleev et al. 2020). It should also be noted that the derivatives defining the right-hand sides in (13) have to be stored as well, and the respective matrix elements are an order in magnitude more numerous than those of $\mathbf{M}_k$. To avoid the memory overflow problem, these elements were recomputed during the adjoint model runs.

In the present study, we found that the variational inversion algorithm based on TLA applications with $K > 3$ iterations, resulted in a very slow decay of the cost function gradient. We attribute this to the strong nonlinearity of the VP sea ice model with respect to the control vector, a significant difference between the true and the first-guess rheological parameters (P^*, e), and the considerable first-guess errors in the initial and open boundary conditions. It was also found that optimization of spatially varying (P^*, e) is efficient only for a relatively short (~1 day) assimilation window. This is due to a 4-times-higher spatial resolution compared to the one (~30 km) utilized by Panteleev et al. (2020) to optimize the rheology of the EVP model, where data assimilation could be efficiently conducted within a ~3–4-day window.

To deal with the problem of slow the convergence, we conducted optimization in several steps: First, the control vector $\mathbf{C} = [\mathbf{C}_0, \mathbf{C}_{\mathrm{OBC}}, \mathbf{C}_p]$ was optimized using a relatively small number of iterations ($K = 3$), which provided only approximate solutions to the nonlinear momentum equation. After obtaining the approximate model trajectory, we gradually increased K up to 10 using the previously optimized control vector $\mathbf{C}$ as a first guess. It was found that each step of such procedure requires about 10–20 solutions of the forward and adjoint models, and thus, the entire minimization required about 50–100 iterative steps, which is comparable to the computational cost of optimizing rheological parameters in the EVP sea ice model (Panteleev et al. 2020).

3. Concept of the observing system simulation experiments

a. OSSE descriptions

Conducting the OSSEs is a first step to analyze the performance and skill of a DA system. These experiments should be performed before applying the DA algorithm to the real observations.

The conventional OSSE methodology (e.g., Nitta 1975; Houtekamer and Mitchell 1998; Francis et al. 2018) includes several steps (see Fig. 1). First, "true" solutions of the sea ice model are generated with a given atmospheric forcing, initial-state conditions, and spatially varying RP's distributions. For the experiments with zonal winds (see below) we specified smooth initial sea ice concentration and thickness distributions and define the initial velocity conditions by a 10–time step (100-min) forward model integration starting from a rest state with all other initial variables and parameters the same. For the experiments with cyclonic winds (see below) all initial conditions and forcing were derived from the model run configured for larger domain.

As a second step, we generated synthetic data by contaminating this true, known solution with spatially correlated noise

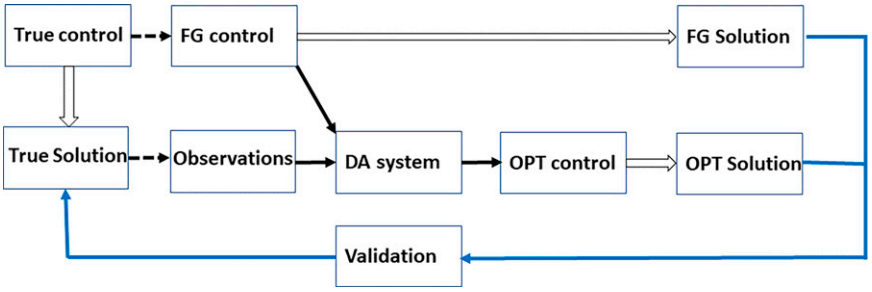

FIG. 1. Schematic of an OSSE. The general process of an OSSE is to generate noisy observations from an a priori natural solution, to assimilate/not assimilate those data into an inaccurately initialized model, and to compare the resulting solutions with the true one. Dashed black arrows correspond to noisy processes, and hollow arrows correspond to application of the forward model. Solid black arrows correspond to system input/output, and the blue arrows identify the quantities compared in the experiment validation. FG, OPT designate the first guess, optimized control, respectively. DA = data assimilation.

whose amplitude and scale depends on the type of observation the data are intended to represent. The level of contamination and spatial/temporal decorrelation scales are discussed below. On the third step, the sea ice model is reinitialized with inaccurate first guess (FG in figures) initial conditions and homogeneous distribution of some of the RPs distributions (e.g., P^* or P^* and e) to mimic the conventional approach with constant rheological parameters P^* and e.

On the fourth step, the variational assimilation scheme presented in section 2 is applied with perfect model assumptions to determine the optimal control $\mathbf{C}_{\text{opt}}$ by assimilating observations during the data assimilation window of 1 day. The optimal model state trajectory and parameters (OPT in figures) result from initialization at the start of day 0.0. Finally, the optimized RP's and sea ice state is compared with "true" sea ice model solution. The latter allows to define the performance and skill of the developed data assimilation algorithm

The major goal of the conducted OSSEs is to evaluate the feasibility of reconstructing the RPs through assimilation of the sea ice velocity, thickness, and concentration observations in the central part of the Arctic Ocean where sea ice concentration is close to 100%

Note also, in pack ice conditions (sea ice concentration $> 97\%$), viscous-plastic rheological forcing in Eq. (1) plays a more important role when sea ice converges [$\text{div}(\mathbf{u}) < 0$], because sea ice divergence will eventually result in the decrease of the sea ice concentration and the exponential decrease of the sea ice pressure P [Eq. (6)], which controls the magnitude of the rheological term in the momentum balance. Note that the impact of the sea ice divergence on the rheological term may be not so straightforward if another rheological hypothesis are applied.

Because of this we consider two types of OSSEs. The first OSSE simulated a rather strong convergence in the entire domain, which was achieved by setting convergent wind from opposite directions and intense inflow of the sea ice into the domain through the western boundary. In the second experiment the domain was forced by the gyre-shaped winds, ocean currents, and open boundary forcing extracted from a larger domain (80×70). As a result, ice convergence was much weaker and changed sign to divergence in some areas. In both OSSEs, we analyze the feasibility of the recovering of the spatially varying P^* with a given distribution of e and, in addition, explore the case when spatial distributions of both P^* and e are unknown and need to be reconstructed. The impact of the higher inaccuracy of the sea ice thickness observations for both OSSEs was also analyzed.

Sea ice pressure term P is also controlled by compactness strength parameter α in the Eq. (6). Note that impact of parameter α is essential only in the regions where sea ice concentration less than 100%. At the same time, any reasonable value (~15–30) of the compactness strength parameter will significantly decrease sea the ice pressure [Eq. (6)] in the regions with sea ice concentration below 90%. That will decrease the impact of the rheological term in the momentum Eq. (1) and make the inversion of RPs inaccurate. Because of that, in order to evaluate the possibility of the inversion of both P^* and α we conducted two additional OSSEs with initial and boundary sea ice concentration multiplied by 0.95. For simplicity, we also suggested that α does not vary in space, i.e., α was an unknown constant, which should be defined together with spatially varying P^*.

A list of the OSSEs with short descriptions is given in Table 2. The maximum number of control variables associated with the initial conditions (the number of ice model grid points occupied by the sea ice thickness, concentration and velocity fields) was about 8000. As it was mentioned above, the RP control fields were defined on a coarser grid ($\Delta x = 10\delta x$) and bilinearly interpolated on the model grid of the respective OSSEs. Thus, the maximum dimension of the RP control vector never exceeded $(50/10 + 1) \times (40/10 + 1)2 = 60$ elements. Here, 50 and 40 are the grid dimensions. In all the experiments, we assumed that sea ice thickness, concentration and velocity observations were available at all the space–time grid points of the model domain. The atmospheric and oceanic forcing fields were contaminated by the large-scale noise, with decorrelation scales of ~150 km. The magnitudes of the respective error fields were ~10% for the ocean and atmosphere.

TABLE 2. List of the performed experiments.

Experiment	Description	Objective	Control
CONV_P	Zonal wind, currents, spatially varying P^*, and known e	Evaluate feasibility of optimizing P^* under strong sea ice convergence	P^*, **u**, h, A
GYRE_P	Cyclonic wind, currents, spatially varying P^*, and known e	Evaluate feasibility of optimizing P^* under weak sea ice convergence	P^*, **u**, h, A
CONV_P_e	Zonal wind, currents, spatially varying P^*, and e	Evaluate feasibility of optimizing P^*, e under strong sea ice convergence	P^*, e, **u**, h, A
GYRE_P_e	Cyclonic wind, currents, spatially varying P^*, and e	Evaluate feasibility of optimizing P^*, e under weak sea ice convergence	P^*, e, **u**, h, A
CONV_P_α	Zonal wind, currents, α, and spatially varying P^*	Evaluate feasibility of optimizing P^*, α under strong sea ice convergence	P^*, α, **u**, h, A
GYRE_P_α	Cyclonic wind, currents, α, and spatially varying P^*	Evaluate feasibility of optimizing P^*, α under weak sea ice convergence	P^*, α, **u**, h, A

b. *Synthetic data*

In all OSSE experiments, we used three types of simulated sea ice observations, trying to keep the magnitude of respective errors close to realistic values, which could be derived from the MOSAiC or similar experiment.

In particular, we adopted rather accurate (0.005 m s^{-1}) sea ice velocity observations for the entire region because the new methods of sequential SAR image comparison can retrieve ice velocities with an accuracy of 0.005 m s^{-1} (Komarov and Barber 2014). Combining these remotely sensed sea ice velocities with the direct observations from sea ice buoys and SAR velocities will likely provide even higher accuracy of the sea ice velocity observations. Thus, in the OSSEs reported below, inaccuracy of sea ice velocities is set to 0.005 m s^{-1}, which corresponds to ~5%–7% of the relative sea ice velocity errors. Similarly, we adopted the same relative error (~5%) of the sea ice concentration observations that are very well observed from multiple satellites, SAR images, and radars. Note that sea ice concentration in the central part of the Arctic Ocean is very close to 100% and because of that, in the most of our experiments, sea ice concentration ranges between 97% and 100% and only in two experiments we reduced sea ice concentration by 5%. Panteleev et al. (2020) showed that the sea ice thickness observations are very important for the proper recovering of the spatially varying rheological parameters. Taking into account that MOSAiC field experiments provide very accurate in situ sea ice thickness observations, we set the sea ice thickness observational error at ~0.1 m, having in mind that multiple buoys and acoustic observations may provide this accuracy for the entire region. We also assumed that all observations are available in all the space–time grid points of the model domain.

4. Optimization of rheological parameters

a. *Optimization of the sea ice strength*

The impact of the sea ice strength on the sea ice state (i.e., velocity, thickness, and concentration) is significantly stronger than the impact of the yield ellipse axes ratio e. To evaluate the feasibility of optimizing P^*, the VP model was configured in a 350 km × 290 km rectangular domain with true values of sea ice thickness at $t = 0$ and 1 day shown in Figs. 2c and 2d. The true values of P^* and e varied as shown in Figs. 2e and 2f with spatial variation in the following ranges: $17.5 \le P^* \le 37.5$ kN m^{-2} and $1.1 \le e \le 2.9$. These ranges were adopted from various studies (e.g., Hibler and Walsh 1982; Kreyscher et al. 1997, 2000; Tremblay and Hakakian 2006; Lemieux et al. 2016). The true wind forcing was blowing from opposite directions with stationary position and strength, gradually increasing 1.2 times during the 1-day assimilation window. The resulting wind at $t = 1$ day is shown in Fig. 2b and has a maximum magnitude of 20 m s^{-1}. The stationary ocean currents were specified as shown in Fig. 2b with a maximum amplitude of 0.1 m s^{-1}, which is a reasonable amplitude for the central part of the Beaufort Sea according to our experiments with CICE6 sea ice model. The zonal open boundary sea ice velocity of 0.2 and 0 m s^{-1} were specified along the western and eastern boundaries, respectively, without any variation in the meridional direction. Along the northern and southern open boundaries, the zonal velocity was interpolated linearly, while the meridional velocity was set to zero at all open boundaries. Note that Dirichlet open boundary conditions are different from Neuman type open boundary conditions utilized by Lemieux et al. (2008). That is because 4Dvar data assimilation minimize the difference between sea ice state and sea ice observations and updates open boundary conditions on each iteration to provide an optimal fit to the data inside the domain. Initial sea ice velocity conditions were determined by a 100-min model integration starting from rest, with all other initial variables and parameters being the same.

This type of forcing and sea ice rheology causes a strong convergence in the entire region with a maximum amplitude of -3.8×10^{-6} s^{-1} (experiment CONV_P in Table 2). The meridional region of strongest convergence along the 120–180 km coincides with minimum in the P^* distribution (Figs. 2a,e) resulting in a substantial (0.25 m) increase of the sea ice thickness in this region from 1.25 m up to 1.5 m in a single day. Sea ice thickness changes in other parts of the domain are less profound, which is probably due to higher P^* and weaker wind

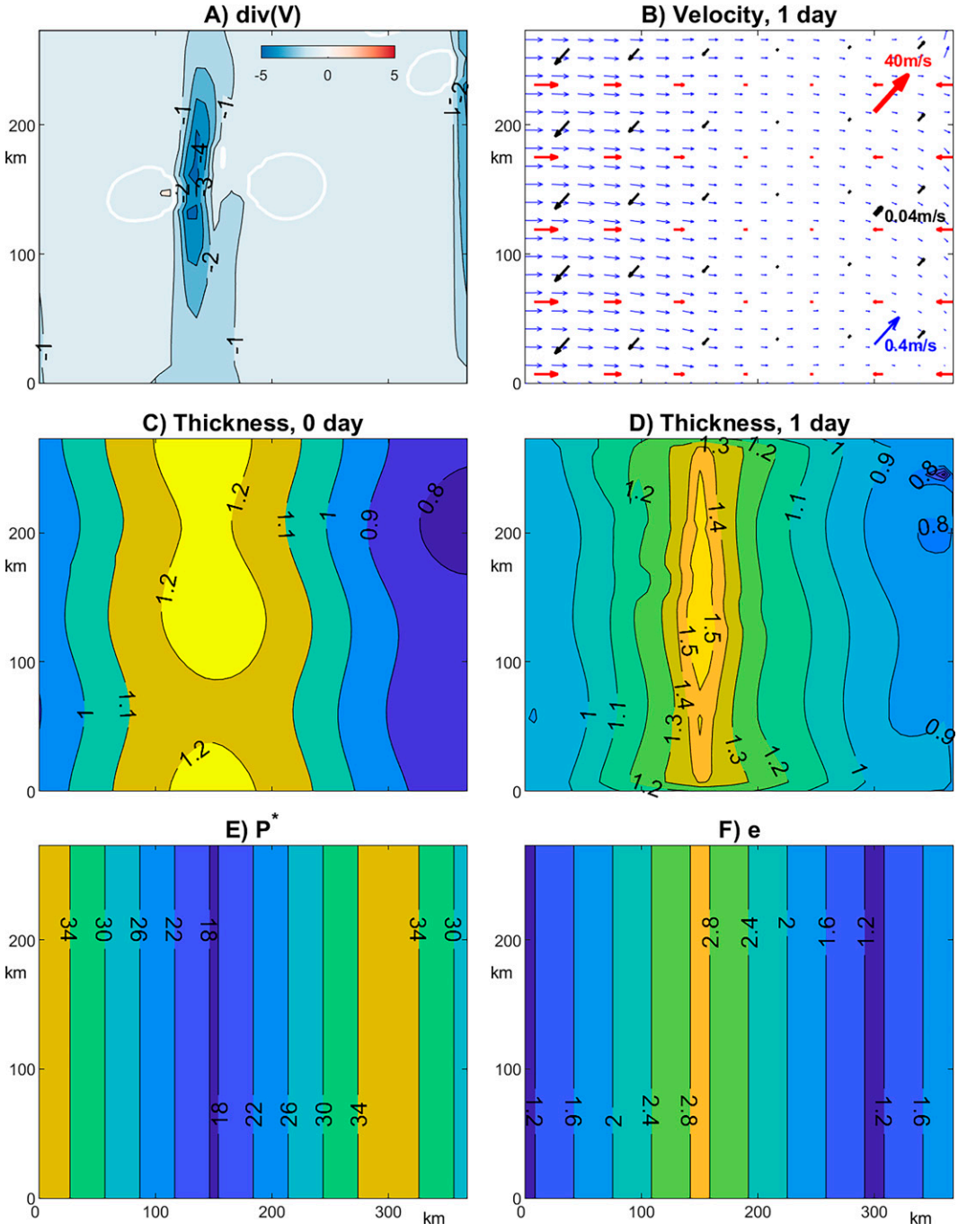

FIG. 2. Parameters of the true solution in the experiments CONV_P and CONV_P_e: (a) div($\mathbf{u}$) ($\times 10^{-6}$ s^{-1}) for the time 0.5 days. White contour corresponds to div($\mathbf{u}$) = 0. (b) Sea ice velocity (blue arrows), wind (red arrows), and ocean currents (black arrows) at $t = 1$ day; (c),(d) sea ice thickness at $t = 0$ and $t = 1$ day; (e),(f) spatial distributions of P^* and e.

forcing. The changes in the sea ice concentration are very moderate because the initial sea ice concentration distribution is close to 100% everywhere. Because of this, the impact of P^* and e optimization on sea ice concentration is not discussed below, although we note that, in all OSSEs, a certain improvement of sea ice concentration distributions was observed.

Noisy sea ice concentration, thickness and velocity observations were generated by adding spatially decorrelated noise (with decorrelation scales of 50 km) to each of the state

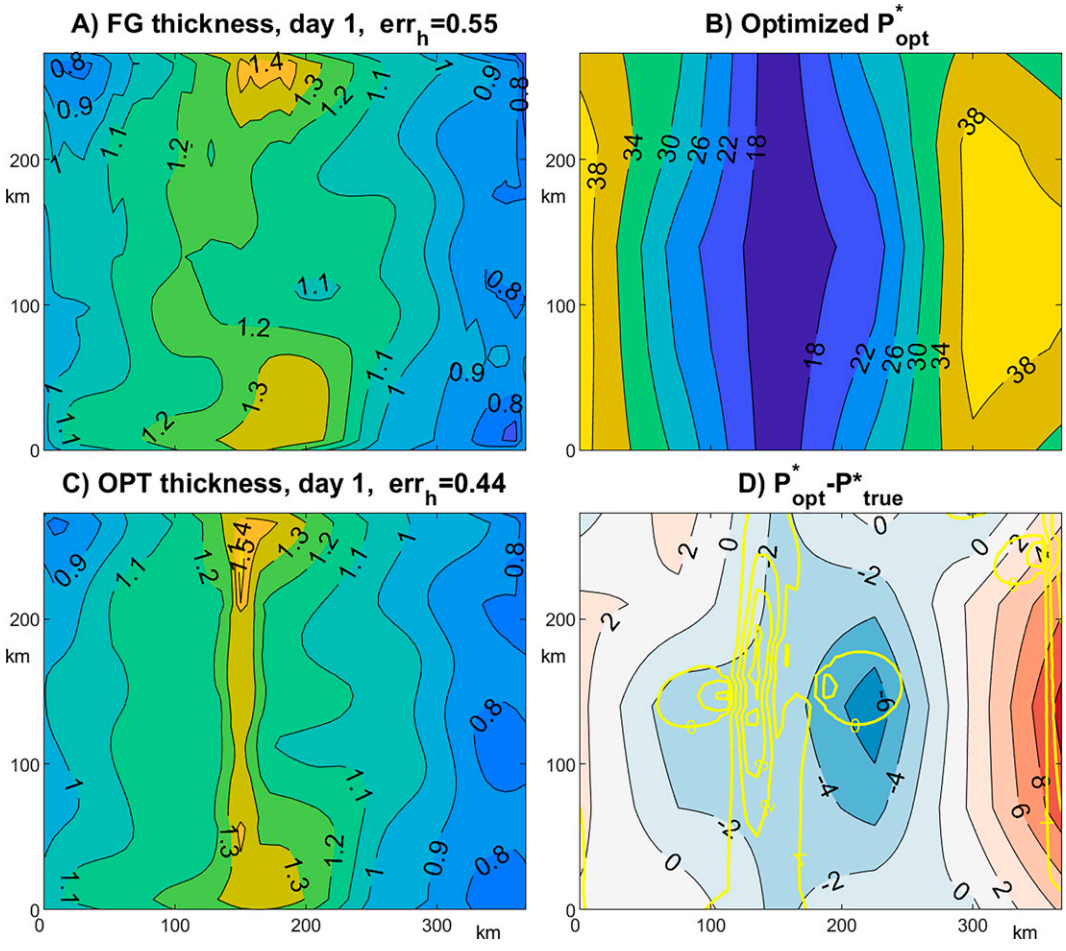

FIG. 3. Results of the CONV_P experiment: (a) sea ice thickness at $t = 1$ day in the first-guess solution; (b) optimized P^*; (c) optimized sea ice thickness at $t = 1$ day. (a),(c) The relative error err_h values; (d) difference between optimized and true P^* Yellow contours show the div(**u**) for the time 0.5 days (see Fig. 2a).

variables at the beginning and at the end of the assimilation window and linearly interpolated in time.

The simulated data mimic realistic observations and errors such as those obtained from sources discussed above. In all the experiments, we did not introduce any bias to ice observations and suggested that sea ice model is also nonbiased. The bias-free hypothesis are common assumptions in most of the existing DA systems. The initial conditions for the first-guess solution were generated in a way similar to the noisy observations, with slightly larger decorrelation length scales for sea ice concentration, thickness, and velocity and spatially uniform values of $P^* = 29.167\ \mathrm{kN\ m^{-2}}$. The wind and ocean forcing were also contaminated, as discussed above. Figure 3a shows that the first-guess sea ice thickness distribution differ significantly from the true sea ice thickness (Fig. 2d) with a relative error of 0.55 estimated as

$$\mathrm{err}_h = \left[\sum(h_{\mathrm{fg}} - h_{\mathrm{true}})^2 \Big/ \sum(h_{\mathrm{true}} - \overline{h}_{\mathrm{true}})^2\right]^{0.5}, \qquad (14)$$

where the overbar denotes the space–time averaging operator. The region of the most profound difference between h_{fg} and h_{true} coincides with the minimum in the true P^* suggesting that the incorrect uniform P^* in the first-guess solution strongly affects the sea ice thickness distribution even for a short (1-day) period of time.

Similarly to Stroh et al. (2019), the optimization was conducted in three steps. First, we optimized initial and open boundary sea ice velocity, thickness, and concentration conditions $[\mathbf{C}_0, \mathbf{C}_{\mathrm{OBC}}]$. Then we sequentially optimized rheological components of the control vector $\mathbf{C}_p$ and finally conducted an additional optimization of the full control vector $\mathbf{C} = [\mathbf{C}_0, \mathbf{C}_{\mathrm{OBC}}, \mathbf{C}_p]$. Note that the simulated sea ice velocity, thickness, and concentration observations efficiently constrain the respective initial conditions and, thus, provide a more accurate first guess for the final optimization of the entire control vector.

Figures 3b and 3d show the optimized P^* distribution which is very close to the true P^* in Fig. 2e. Note that our optimization succeeded in a good reconstruction of the minimum in P^* along the 150-km meridian, while the shape of the maximum along the 300-km meridian was reconstructed with higher errors. This is due to weaker sea ice convergence in these regions and

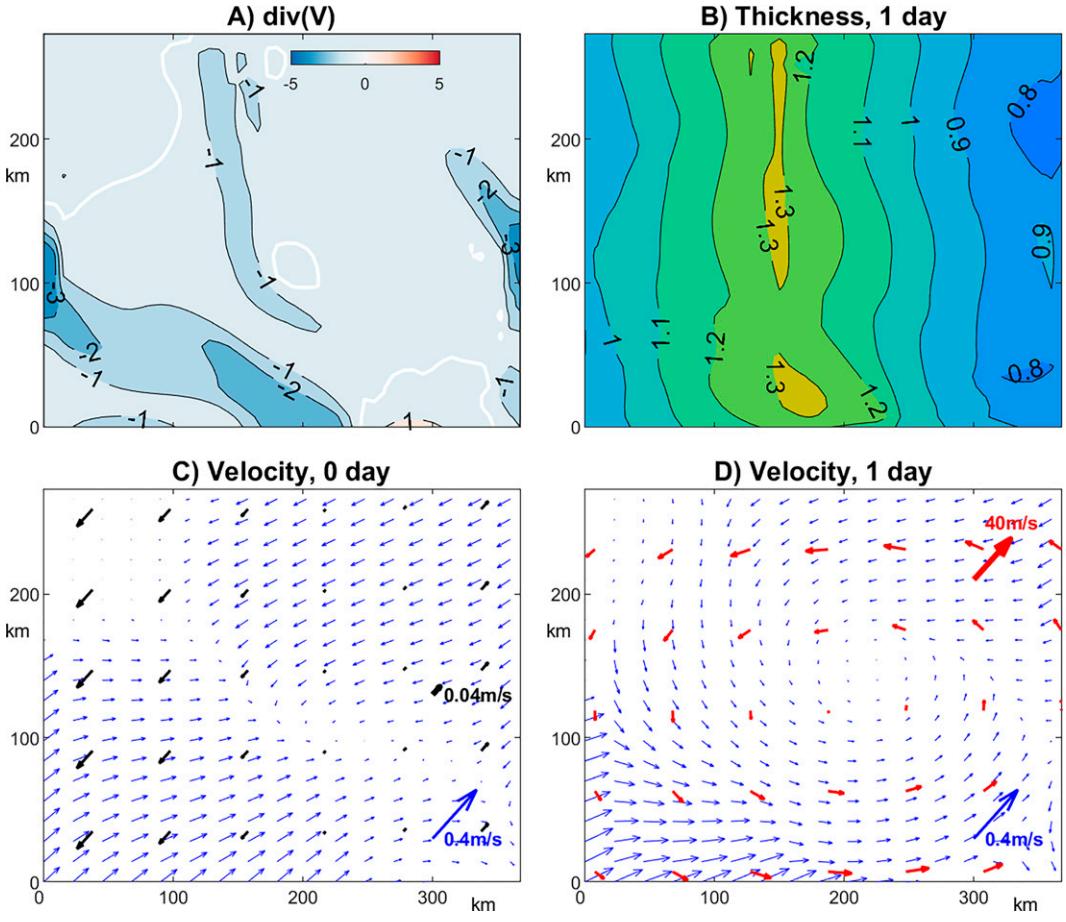

FIG. 4. True solution in the experiments GYRE_P and GYRE_P_e: (a) div (**u**) (10^{-6} s^{-1}) for $t = 0.5$ days. White contour corresponds to div(**u**) = 0. (b) Sea ice thickness at $t = 1$ day; (c),(d) blue arrows—sea ice velocities at $t = 0$ and $t = 1$ day. Red and black arrows show the wind and ocean currents.

less impact of the rheological term on the local ice dynamics (Fig. 3d). The optimization of the spatial distribution of P^* results in a significant improvement in the sea ice thickness distribution and a reduction of relative errors of up to 0.24 (Fig. 3c).

Interestingly, that maxima of h_{opt} (1.5 m) is slightly smaller than maximum in h_{true} distributions (1.6 m) due to wider area with minimum P^* along 150-km meridian. There is a slight (0.05-m) difference between h_{opt} and h_{true} in another area of the model domain. Again, this is due to the better reconstruction of the minimum in P^*. There is also a significant improvement in the optimized velocity field $\overline{[(u_{opt} - u_{true})^2 + (v_{opt} - v_{true})^2]}^{0.5} = 0.01\ m\ s^{-1}$ with respect to the first-guess velocity fields $\overline{[(u_{fg} - u_{true})^2 + (v_{fg} - v_{true})^2]}^{0.5} = 0.03\ m\ s^{-1}$.

The opposite wind forcing over the 350-km domain cannot be considered as a typical environmental condition in the central Arctic, so, we conducted a GYRE_P experiment with a more realistic gyre-like cyclonic wind and open boundary conditions, extracted from the sea ice model solution, configured for a larger domain. The initial/open boundary sea ice concentration was set to 1 everywhere, while the initial/open boundary sea ice thickness, ocean currents, P^*, and e were the same as in CONV_P experiment (Fig. 2). The gyre-like wind has a maximum magnitude of 18 m s^{-1} at the beginning of the assimilation window and gradually increases to 22 m s^{-1} by the end of model integration (Figs. 4c,d). Under such forcing, sea ice rotates counterclockwise, with a maximum speed of 0.13 m s^{-1} at the beginning and 0.21 m s^{-1} at the end of model integration period (Figs. 4c,d). Similarly to the CONV_P experiment, sea ice converged in most parts of the domain, with a maximum convergence of $\sim -2 \times 10^{-6}$ s^{-1}, which correlates well with the minimum in the P^* distribution. However, there were also substantial areas where the sea ice weakly diverged. The resulting sea ice thickness distribution indicates an increase by 0.15 m, in the center, due to sea ice convergence (Fig. 4b).

The observations and the first-guess control vector were set in the same way as in the CONV_P experiment; i.e., P^*_{fg} was set to 29.167 kN m^{-2}. The first-guess sea ice thickness, by the end of the period of integration, is relatively smooth (Fig. 5a) and does not have the maximum along the 150 km meridian,

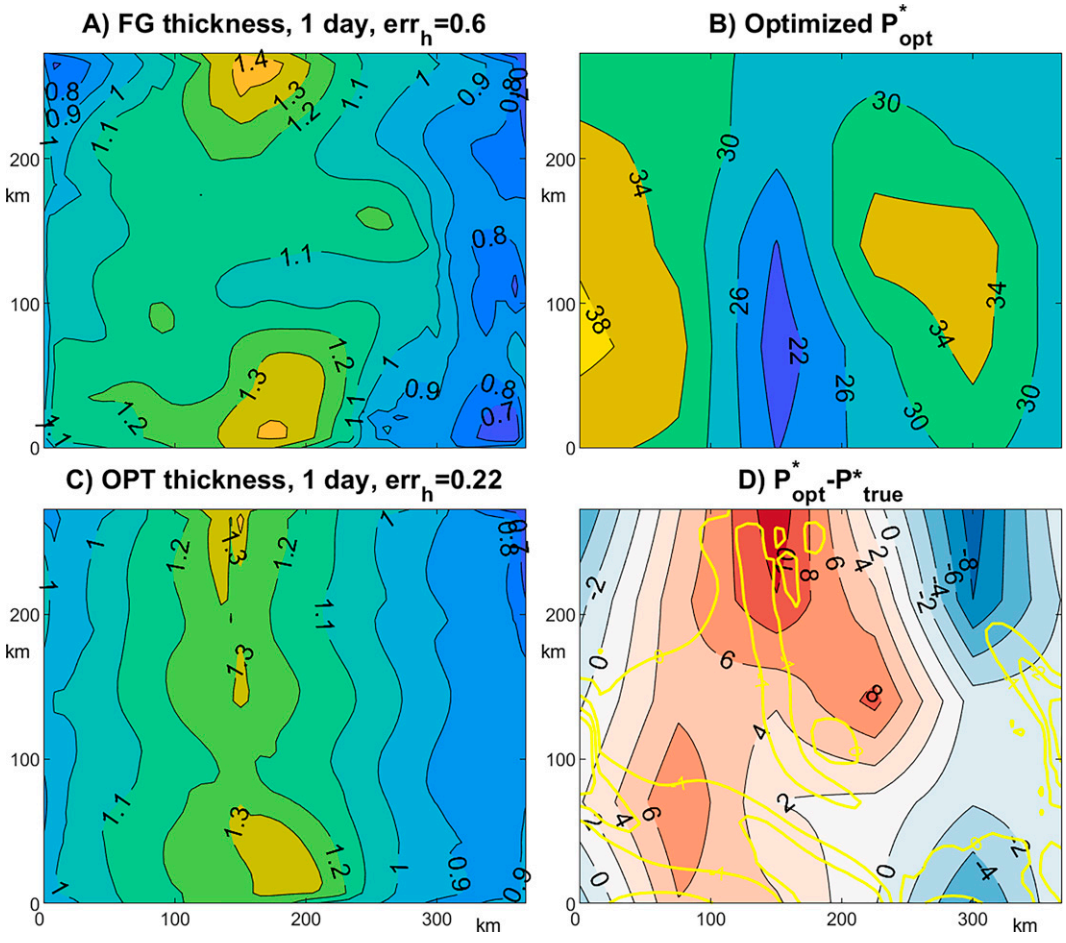

FIG. 5. Results of the GYRE_P experiment: (a) sea ice thickness at $t = 1$ day in the first-guess solution; (b) optimized P^* ; (c) optimized sea ice thickness at $t = 1$ day. (a),(c) The relative error magnitudes err_h; (d) difference between optimized and true P^* Yellow contours show the div(**u**) (see Fig. 4a).

which is clearly seen in the true solution (Fig. 4b). This is due to a uniform P^*_{fg}. Optimization was conducted in a similar manner as described above and Fig. 5b shows the optimized P^*_{opt} distribution. A comparison with the true P^*_{true} (Figs. 5d, 2e) reveals some difference along the northern and southern boundaries, but, in the central part of the domain, the P^*_{opt} P^*_{opt} has the same configuration of maxima and minima and their absolute values as P^*_{true} distribution. The optimization of P^*_{opt} also provides significantly more accurate optimized sea ice thickness distribution (Fig. 5c) which now has several maxima whose position coincides with the positions of the maxima in the true sea ice thickness field (Fig. 4b).

To evaluate the impact of the inaccuracy of the sea ice thickness observations, we conducted a series of CONV_P and GYRE_P experiments, gradually increasing the relative noise in the sea ice thickness observations and evaluating the difference between P^*_{opt} and P^*_{true}, $d_p^{\mathrm{opt}} = \overline{(P^*_{\mathrm{opt}} - P^*_{\mathrm{true}})^2}^{0.5}$. The results in Table 3 show that decreasing the accuracy of the sea ice thickness observations results in significant degradation of the P^*_{opt} distribution. However, taking into account that spatial variability of P^*_{true} is $d_p^{\mathrm{true}} = \mathrm{std}(P^*_{\mathrm{true}}) = \overline{(P^*_{\mathrm{true}} - \overline{P^*_{\mathrm{true}}})^2}^{0.5} = 5.77\ \mathrm{kN\ m^{-2}}$, even relatively high sea ice thickness (~0.2 m) errors allow satisfactory reconstruction of the P^*_{opt}, even in the case of the realistic GYRE_P experiment with cyclonic wind. Naturally, the reconstruction errors are nearly 2 times smaller than those obtained in the experiment with strong convergence (CONV_P).

b. *Optimization of the sea ice strength and yield curve axes ratio*

The yield curve axes e is another important rheological parameter, which can formally be reconstructed through

TABLE 3. d_p^{opt} (N m^{-2}) as a function of std($h_{\mathrm{opt}} - h_{\mathrm{true}}$) in the sea ice thickness observations. d_p^{opt} is shown in the last column.

Experiment	std$_h$ = 0.09 m	std$_h$ = 0.18 m	std$_h$ = 0.3 m	std(P^*_{true})
CONV_P	2.3×10^3	2.6×10^3	3.3×10^3	5.77×10^3
GYRE_P	4.3×10^3	4.5×10^3	6.2×10^3	5.77×10^3

4Dvar. However, the impact of this parameter on the rheological term in the momentum Eq. (1) is much weaker than the impact of P^*, because σ_{ij} is directly proportional to P^* [see Eqs. (4), (6), and (8)]. To evaluate the feasibility of optimizing spatially varying P^* and e, we conducted two additional OSSEs (CONV_P_e and GYRE_P_e), and set P^* and e to be spatially homogeneous in the first-guess solution. Observational errors, contamination of the first-guess solution with large-scale noise and inaccuracy in the ocean currents and atmospheric forcings were set in a similar manner as in the experiments CONV_P and GYRE_P, discussed above. Optimization of two unknown distributions was conducted in a sequential manner; i.e., we initially optimized spatially varying P^*, then spatially varying e, and finally conducted the optimization of the entire control vector $\mathbf{C} = [\mathbf{C}_0, \mathbf{C}_{\mathrm{OBC}}, \mathbf{C}_p]$.

The major results of the CONV_P_e experiment are shown in Fig. 6. The optimization clearly provided a reasonable estimate of P^* (Fig. 6a), with $d_p^{\mathrm{opt}} = 2.4\ \mathrm{kN\ m^{-2}}$. The difference between $P^*_{\mathrm{opt}} - P^*_{\mathrm{true}}$ is shown in Fig. 6c. This accuracy is comparable with the results of the CONV_P experiment, with twice less accurate sea ice thickness observations (Table 3), but still much smaller than the standard deviation $\mathrm{std}(p^*_{\mathrm{true}}) = 5.77\ \mathrm{kN\ m^{-2}}$. The quality of the reconstruction of e is not so successful (Figs. 6b,d). The d_e^{opt} between optimized and true e is about 0.89, which is larger than $\mathrm{std}(e_{\mathrm{true}}) = \overline{(e_{\mathrm{true}} - \overline{e_{\mathrm{true}}})^2}^{0.5} = 0.52$. Note, however, that the major inaccuracies in e_{opt} are in the eastern and western parts of the domain (Fig. 6d), while the strong meridional maximum in the vicinity of 150-km meridian agrees well with the true e_{true} distribution. This is due to strong ice convergence in this region of the true solution (Fig. 2a) which results in a stronger impact of the rheological term in the momentum balance [Eq. (1)].

Despite the inaccuracies in the reconstructed P^*_{opt} and especially e_{opt}, the optimized sea ice thickness distribution (Fig. 6f) demonstrates a strong resemblance to the true sea ice thickness (Fig. 2d), with a relative error of 0.33, which is about 1.5 larger than the relative errors in the CONV_P experiment. This is due to the stronger impact of P^* on the sea ice dynamics and the relatively accurate reconstruction of P^*_{opt}.

The major results of the GYRE_P_e experiment are shown in Fig. 7. Due to the weaker sea ice convergence, the reconstruction of P^* is not as accurate as in the CONV_P_e experiment; however, the $d_p^{\mathrm{opt}} = 25.3\ \mathrm{kN\ m^{-2}}$ is still smaller: $\mathrm{std}(p^*_{\mathrm{true}}) = 5.8\ \mathrm{kN\ m^{-2}}$, and there is a clear similarity with the true solution in the locations at the maxima and minima along the 150 and 300 km meridians, respectively (Fig. 2e). This similarity agrees well with the minima in $(P^*_{\mathrm{opt}} - P^*_{\mathrm{true}})$ distribution shown in Fig. 7c.

The d_e^{opt} between the optimized and true e is about 0.4, which is slightly smaller than $\mathrm{std}\ (e_{\mathrm{true}}) = 0.52$. There is also some portion of similarity between optimized e_{opt} and true e_{true} distributions: for example, in locations of the minima along the western and eastern boundaries and of the maximum in the central part of the domain. This similarity agrees well with the minima in $(e_{\mathrm{opt}} - e_{\mathrm{true}})$ distribution shown in Fig. 7d.

Due to partial optimization of P^*_{opt} and e_{opt}, the optimized sea ice thickness distribution (Fig. 7d) also demonstrates some improvements with respect to the first-guess sea ice thickness and the reduction of the relative error from 0.6 up to 0.4 (Figs. 7c,d). Overall, the results of both experiments CONV_P_e and GYRE_P_e indicate the feasibility of reconstructing the spatially varying P^* distribution and a somewhat less accurate reconstruction of the spatially varying e distribution.

c. *Optimization of the sea ice strength and compactness strength parameter*

The compactness strength parameter α is the second parameter which defines the sea ice pressure in Eq. (6). In the regions entirely covered by sea ice, the impact of the compactness strength parameter is negligible, but it can be comparable or even increase the impact of the P^* in the regions where sea ice concentration varies between 90% and 100%. With smaller sea ice concentration the impact of the rheological term in Eq. (1) significantly decreases. In many sea ice model applications α is equal to 20, but some studies suggest that it could be smaller and may significantly impact the sea ice dynamics in the models (e.g., Ungermann and Losch 2018).

Because of that we conducted two OSSEs with strong convergence (CONV_p_α) and cyclonic wind (GYRE_p_α) and evaluated the possibility to define both P^* and α assuming that e is known. Taking into account that α is the dimensionless parameter, which defines the impact of the sea ice concentration on the sea ice pressure we assumed that α is unknown and its value does not vary in space. The true P^* distribution of sea ice velocity and sea ice thickness were the same as in other OSSEs, while initial sea ice concentration was multiplied by 0.95. In the first-guess solution we specified $\alpha_{\mathrm{fg}} = 25$ and uniform P^*. Forcing was the same as in other OSSEs. Optimization was conducted in 3 steps as described above. We also found that optimization of α during the first step accelerates convergence providing more accurate reconstruction. That is probably due to small dimension of the $\mathbf{C}_\alpha$ control, but also could be due to strong impact of the α in the region with 95% of the sea ice concentration. Results of the optimization are shown in Fig. 8.

Both OSSEs demonstrated the reasonable accuracy (i.e., d_p^{opt}) of P^* reconstruction, which was smaller the correspondent spatial variability of the P^*_{true} (Figs. 8a,b). The accuracy of the reconstructed P^*_{opt} in the CONV_P_α experiment is smaller then P^*_{opt} in the GYRE_P_α and clear reveal similar maximum and minimums as in the P^*_{true} (Fig. 8a). The errors have a clear minimum along the 150 km suggesting that open boundaries may impact the results of the retrievals. Note that the OSSE with strong sea ice convergence allowed rather accurate $\alpha = 20.8$, while optimized α in the GYRE_P_α experiment was equal 22.9. Overall, both experiments demonstrate the possibility to retrieve P^* and α from observations of the sea ice velocity, thickness, and concentration, but results will be more accurate in the case of the stronger sea ice convergence. We also found that accuracy of the retrievals of both P^* and α significantly decreases if initial sea ice concentration becomes less than 90%.

5. Discussion and conclusions

The presented study is an extension of our previous effort (Panteleev et al. 2020) and addresses the feasibility of retrieving

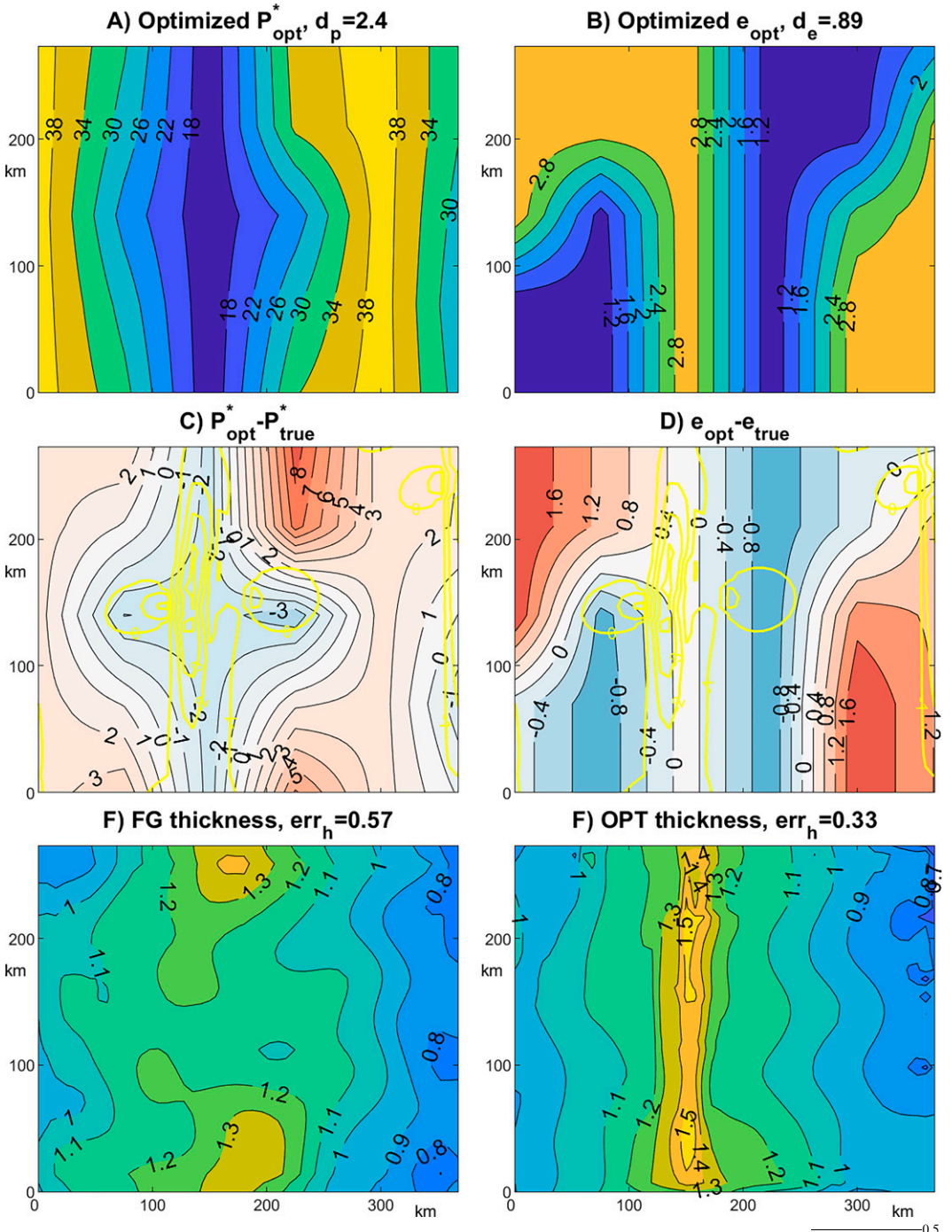

FIG. 6. Results of the CONV_P_e experiment. (top) Optimized (a) P^* and (b) e distributions. $d_p^{\text{opt}} = 10^{-3}\overline{(P^*_{\text{opt}} - P^*_{\text{true}})^2}^{0.5}$ and $d_e^{\text{opt}} = \overline{(e_{\text{opt}} - e_{\text{true}})^2}^{0.5}$ are shown on each panel. (middle) Difference between optimized and true (c) P^* and (d) e. Yellow contours show the div(**u**) for the time 0.5 days (see Fig. 2a). (bottom) Sea ice thickness at $t = 1$ day in the (e) first-guess and (f) optimized solutions. The relative error magnitudes err_h are shown in (e) and (f).

spatially varying RPs through 4Dvar assimilation of satellite observations of sea ice velocity, thickness, and concentration using the VP sea ice model. To do the analysis, we developed TLA codes with respect to all rheological parameters, initial conditions, wind and oceanic forcing for a single-category sea ice model proposed by Lemieux et al. (2008). The dynamical core of this model is based on conventional formulation of the VP rheology (Hibler 1979), and parameterizations of the grounding and arching of

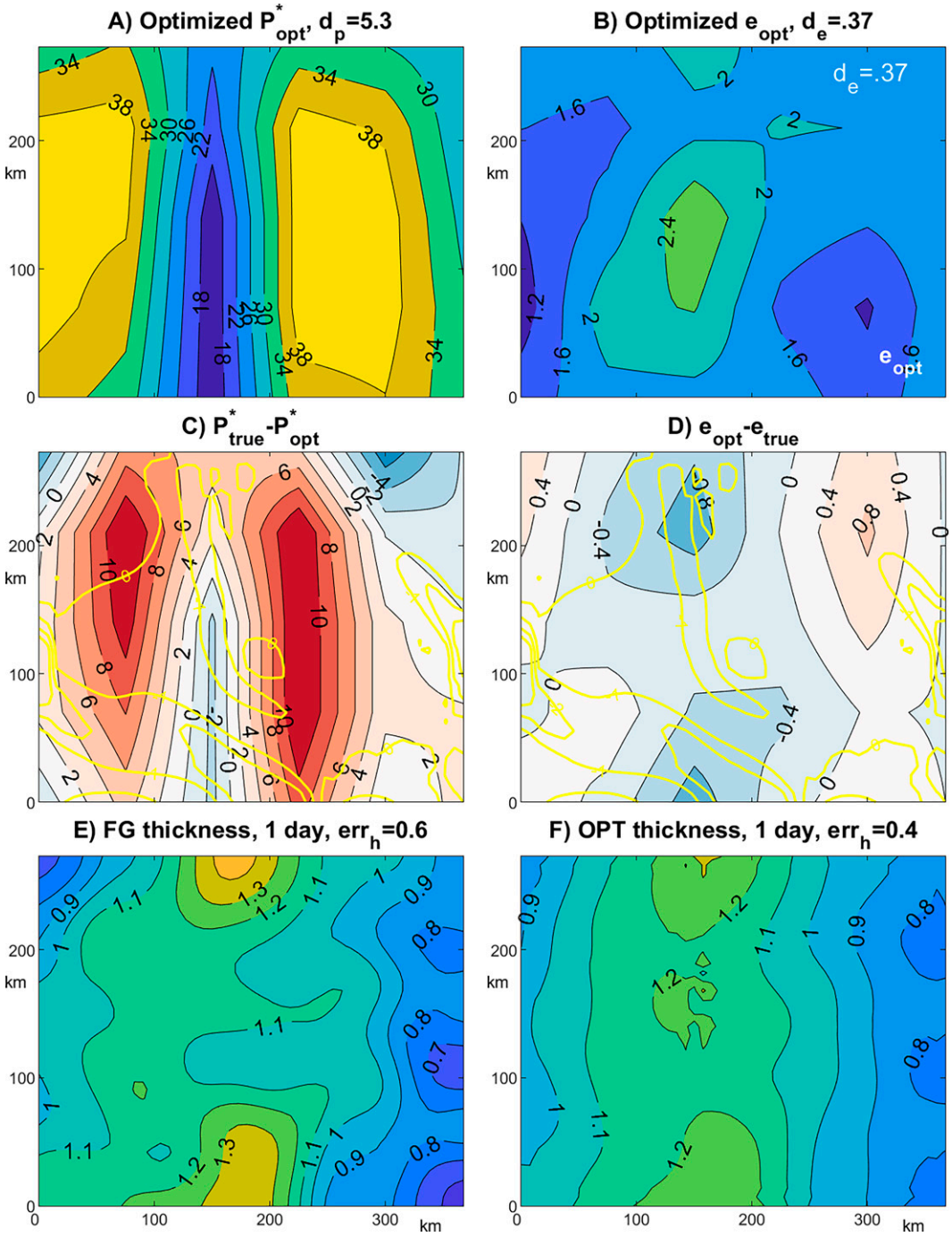

FIG. 7. Results of the GYRE_P_e experiment. (top) Optimized (a) P^* and (b) e distributions. $d_p^{\text{opt}} = 10^{-3}\overline{(P^*_{\text{opt}} - P^*_{\text{true}})^2}^{0.5}$ and $d_e^{\text{opt}} = \overline{(e_{\text{opt}} - e_{\text{true}})^2}^{0.5}$ are shown. (middle) Difference between the optimized and true (c) P^* and (d) e. Yellow contours show the div(**u**) for the time 0.5 days (see Fig. 4a). (bottom) Sea ice thickness at $t = 1$ day of the (e) first-guess and (f) optimized solutions. The relative error magnitudes err_h are shown in (e) and (f).

land fast ice proposed by Lemieux et al. (2015, 2016) and König Beatty and Holland (2010). The numerical formulation of the model is similar to the one proposed by Lemieux et al. (2008), but our model is formulated on the B grid and utilizes the GMRES solver with a built-in incomplete LU factorization with a dual truncation strategy (Saad 2003). We also employed a simplified nonlinear Lax–Wendroff scheme for ice advection. This simplification was adopted to reduce complexity of the TLA

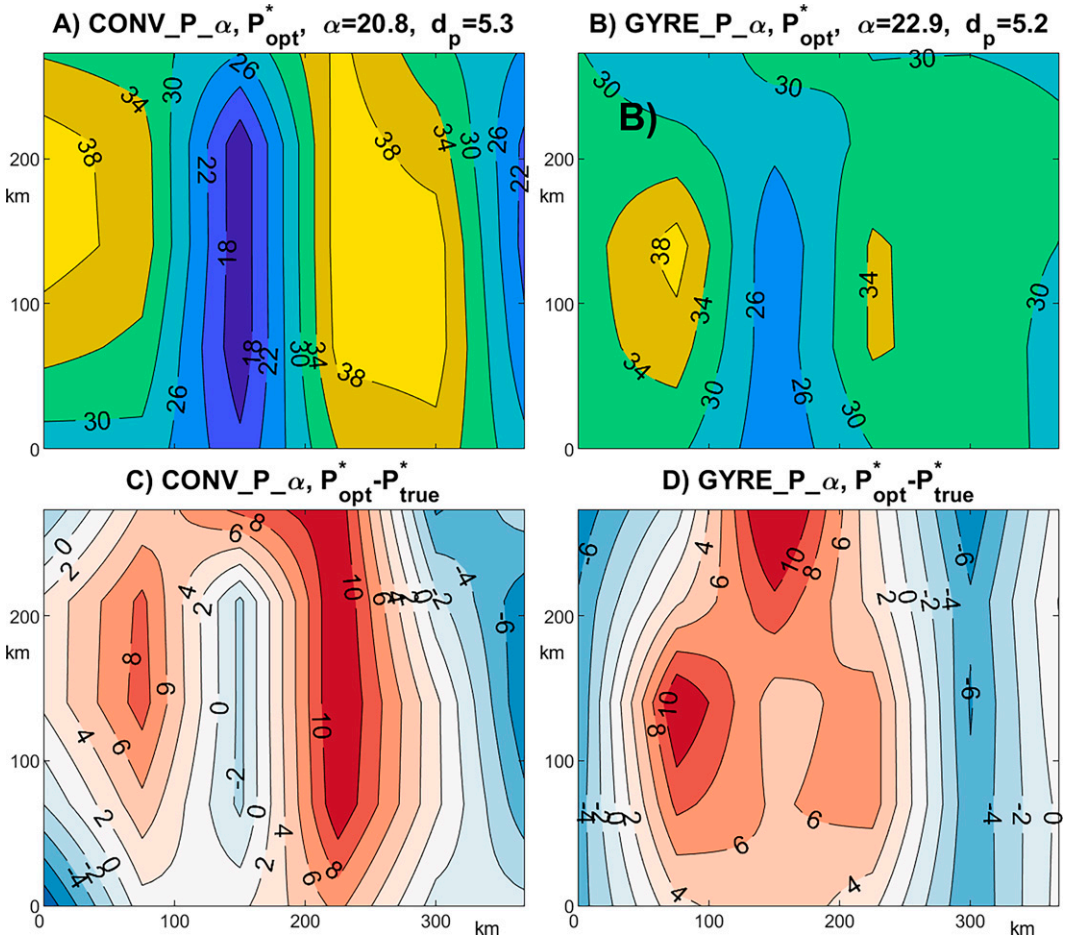

FIG. 8. (top) Optimized P^* distributions for (a) CONV_P_α and (b) GYRE_P_α experiments. The reconstructed values of α and $d_p^{\text{opt}} = 10^{-3}\overline{(P^*_{\text{opt}} - P^*_{\text{true}})^2}^{0.5}$ are shown on each penl. (bottom) Difference between the optimized and true P^* for the (c) CONV_P_α and (d) GYRE_P_α experiments.

codes, and it had negligible impact on the results at the 1-day time scale of the assimilation experiments.

The TLA model for the VP solver was stable and does not require the regularization needed for the EVP TLA model (Panteleev et al. 2020). However, the strong nonlinearity of the VP solver, with multiple outer iterations, provides a limitation on the accuracy of the TL approximation and the length of the DA window. Using the VP model and 4Dvar algorithm, we explore the feasibility of reconstructing a spatially varying RP in the model domain, with high (7-km) resolution, and intensive forcing, through the open boundaries, for atmospheric wind and oceanic currents and sea surface slope.

Our sea ice model does not include thermodynamic forcing, but our numerical experiments with CICE6 sea ice model show that in winter during a period of 1–2 days the contribution to sea ice thickness caused by thermodynamic forcing does not exceed 1–2 cm when the mean sea ice thickness about 1–1.5 m. Taking into account Eq. (6) the thermodynamic processes will contribute only 1%–2% to the sea ice pressure, which is equivalent to the difference in P^* of about 200–500 N m^{-2}, i.e., much smaller the typical spatial variation of the P^* field. Thus, the impact of the thermodynamic forcing is negligible for the data assimilation window of 1–2 days and probably even more days.

In the first two OSSEs we reconstructed spatially varying sea ice strength P^* under the assumption that the distribution of yield curve axes ratio e is known. It was shown that, in the case of strong sea ice convergence, the 4Dvar approach allows for a rather accurate reconstruction of P^* with a d_p^{opt} of 2.4 kN m^{-2}. In a more realistic setting, with weaker wind convergence, the accuracy degrades down to 4.3 kN m^{-2}, still 1.4 times smaller than spatial variability of the P^*_{true} distribution (5.77 kN m^{-2}). We also analyze the impact of the relative accuracy of the sea ice thickness observations and demonstrated robustness of the 4Dvar DA algorithm in recovering reasonable estimates of the P^* distribution.

In two additional OSSEs with strong and weak convergence, we adopted unknown spatial distributions of both the sea ice strength P^* and the yield curve axes ratio e. It was found in that case that the 4Dvar algorithm still allows for a

relatively accurate optimization of P^* and a much less accurate e distribution. However, there is still a significant qualitative similarity between the true e_{true} and the reconstructed e_{opt} distributions, especially in the regions with strong sea ice convergence. In all the experiments, it was also found that the optimization of the rheological parameters significantly improves the sea ice thickness distribution suggesting that proper optimization of the RPs may improve the accuracy of the short-range sea ice forecast. The impact of the properly optimized P^* distribution on the accuracy of the reconstructed sea ice thickness is the most profound, in comparison to the impact of the spatially varying e distribution. Similar results were obtained for the EVP sea ice model (Panteleev et al. 2020).

In two final OSSEs, we analyze the possibility of the reconstruction of the maximum sea ice strength P^* and compactness strength parameter α. Our results indicate that reasonable reconstruction quality of both parameters is possible for the sea ice concentration between 90% and ~98%. As in other OSSEs retrievals of P^* and α are more accurate for the experiment with stronger convergence. For convenience, all final results of the conducted OSSEs are assembled in Table 4.

The conducted OSSEs can be used for developing an optimal strategy for processing observations collected in the central part of the Arctic Ocean, in the framework of the MOSAiC expedition or similar experiments conducted from drifting sea ice. The first step should include a preliminary analysis of the sea ice velocity observations and identification of the periods of intense sea ice convergence and 100% concentration. After that, 4Dvar DA algorithms can be applied for optimizing the spatially varying P^* distribution, with a set of different uniform distributions of (x, y), in order to optimize P^* and derive the most probable values of the mean e for the observed sea ice conditions. Using these values as a first guess, we may try to reconstruct the spatial variability of e for time periods of stronger sea ice convergence. If we assume that the rheological parameters are stable for a certain period of time, optimization may be conducted simultaneously for several data assimilation windows using the same RPs control, and previously optimized initial and open boundary conditions.

In the present study, we utilized realistic observational errors for sea ice velocity, thickness, and concentration error levels were assumed to be characteristic for extensive in situ studies, like the recently accomplished MOSAiC expedition. The OSSEs were configured at a higher resolution to capture significant RP variability in the ridging areas. At the same time, the variational approach can be applied for the experiment with less accurate and dense sea ice observations. In this case, one needs to increase the model resolution and reduce the number of parameters controlling the RP distribution. In the present study, RPs were assumed to depend on spatial coordinates only. However, if we assume that RPs represent intrinsic sea ice properties, poorly described by the heuristic Eq. (6), it could be worth exploring the impact of the advection in the RP fields, which can be described by an additional equation similar to Eqs. (2) and (3). Analysis of the potential impact of incorporating a temporal dependence of the RPs, and the application of the current 4Dvar algorithm to the real sea ice observations, will be within the focus of our studies in the near future.

TABLE 4. The first-guess and optimized metrics dP^*_{fg}, dP^*_{opt}, de_{fg}, e_{opt}, err_h^{fg}, and err_h^{opt} for discussed OSSEs.

Experiment	dP^*_{fg}	dP^*_{opt}	de_{fg}	de_{opt}	err_h^{fg}	err_h^{opt}
CONV_P	5.77	2.3	0	0	0.55	0.44
GYRE_P	5.77	4.3	0	0	0.6	0.22
CONV_P_e	5.77	2.4	0.52	0.89	0.57	0.33
GYRE_P_e	5.77	5.3	0.52	0.37	0.6	0.4
CONV_P_α	5.77	5.3	0	0	0.59	0.32
GYRE_P_α	5.77	5.2	0	0	0.67	0.20

Thus, in coarse-resolution mode the presented approach may be applied to the multiple datasets collected around the multiple moorings installed in the Arctic Ocean during the last decade in the Beaufort Sea (Beaufort Gyre Exploration Project; https://www2.whoi.edu/site/beaufortgyre/methods/instruments/) and along the Siberian continental shelf (Nansen and Amundsen Basins Observational System; https://uaf-iarc.org/nabos/). Inversion of the in situ and satellite observations from these moorings may be helpful for analysis of the spatial and temporal variability of the basic rheological parameters. Once defined, this variability may be considered in the climatological sea ice model.

The proposed 4Dvar technique could be also adopted for more complicated sea ice models. After that, the adjustment of the RP's can be used for the improvement of the short-range sea ice forecast through the optimization of the most important RP's. Besides the improved estimates of the sea ice state (velocity, concentration, and thickness), that should increase the accuracy of the short-range forecast of the linear kinematic features, which are strongly controlled by the spatially varying P^*.

For our study we adopted conventional OSSE approach where observations are generated from a "true" run of the utilized VP sea ice model. Thus, we inherently assume that VP rheology describes the true behavior of the sea ice. This is a rather strong assumption because realistic sea ice behavior is defined by complex interactions between sea ice floes and should also take into account the processes of the sea ice damaging and healing. Thus, the real process of the sea ice ridging is more complicated than the simple increase of the sea ice thickness and concentration described in VP (or EVP) sea ice models. Thus, if applied to the real application the proposed approach will provide the estimates of the RPs which will correspond to the most accurate VP approximation of the real behavior of sea ice fields. An approach could be also considered as a first step in the development of the similar algorithm for the more physically based and sophisticated models (e.g., Tremblay and Mysak 1997; Dansereau et al. 2016).

Acknowledgments. The NRL authors were supported by the Office of Naval Research Program Elements 0603207N29 (Navy Earth System Prediction Capability) and 0602435N (Arctic Data Assimilation). Oceana Francis was supported

by the Coastal Hydraulics Engineering Resilience (CHER) Lab, the Civil and Environmental Engineering Department, and the Sea Grant College Program at the University of Hawai'i at Mānoa.

Data availability statement. All inputs to the model experiments are from idealized conditions as specified in the paper. The numerical scheme practically repeats numerical scheme proposed by Lemieux et al. (2008) and can be easily replicated. Model results in this study are securely stored at the Navy DSRC archive server and can be accessed after obtaining an account at the facility. The corresponding author can be contacted for information to access the archived data once an account has been established.

REFERENCES

Alexandrov, V., S. Sandven, J. Wahlin, and O. M. Johannessen, 2010: The relation between sea ice thickness and freeboard in the Arctic. *Cryosphere*, **4**, 373–380, https://doi.org/10.5194/tc-4-373-2010.

Anderson, D. L., and W. F. Weeks, 1958: A theoretical analysis of sea-ice strength. *Eos, Trans. Amer. Geophys. Union*, **39**, 632–640, https://doi.org/10.1029/TR039i004p00632.

Arnold, C. P., Jr., and C. H. Dey, 1986: Observing system simulation experiments: Past, present, and future. *Bull. Amer. Meteor. Soc.*, **67**, 687–695, https://doi.org/10.1175/1520-0477(1986)067<0687:OSSEPP>2.0.CO;2.

Bennett, A. F., 1992: *Inverse Methods in Physical Oceanography*. Cambridge University Press, 346 pp.

Dansereau, V., J. Weiss, P. Saramito, and P. Lattes, 2016: A Maxwell elasto-brittle rheology for sea ice modelling. *Cryosphere*, **10**, 1339–1359, https://doi.org/10.5194/tc-10-1339-2016.

Errico, R. M., 1997: What is an adjoint model? *Bull. Amer. Meteor. Soc.*, **78**, 2577–2591, https://doi.org/10.1175/1520-0477(1997)078<2577:WIAAM>2.0.CO;2.

Francis O., G. Panteleev, M. Yaremchuk, V. Luchin, J. Stroh, P. Posey, and D. Hebert, 2018: Observing system simulation experiments and adjoint sensitivity analysis: Methods for observational programs in the Arctic Ocean. *Arctic*, **71** (Suppl.), 1–14, https://doi.org/10.14430/arctic4603.

Giering, R., and T. Kaminski, 1998: Recipes for adjoint code construction. *ACM Trans. Math. Software*, **24**, 437–474, https://doi.org/10.1145/293686.293695.

Goldberg, D. N., and P. Heimbach, 2013: Parameter and state estimation with a time-dependent adjoint marine ice sheet model. *Cryosphere*, **7**, 1659–1678, https://doi.org/10.5194/tc-7-1659-2013.

Harder, M., and H. Fischer, 1999: Sea ice dynamics in the Weddell Sea simulated with an optimized model. *J. Geophys. Res.*, **104**, 11 151–11 162, https://doi.org/10.1029/1999JC900047.

Heimbach, P., D. Menemenlis, M. Losch, J.-M. Campin, and C. Hill, 2010: On the formulation of sea-ice models. Part 2: Lessons from multi-year adjoint sea ice export sensitivities through the Canadian Arctic Archipelago. *Ocean Modell.*, **33**, 145–158, https://doi.org/10.1016/j.ocemod.2010.02.002.

Herman, A., 2016: Discrete-Element bonded-particle Sea Ice model DESIgn, version 1.3a—Model description and implementation. *Geosci. Model Dev.*, **9**, 1219–1241, https://doi.org/10.5194/gmd-9-1219-2016.

Hibler, W. D., 1979: A dynamic thermodynamic sea ice model. *J. Phys. Oceanogr.*, **9**, 815–846, https://doi.org/10.1175/1520-0485(1979)009<0815:ADTSIM>2.0.CO;2.

——, and J. E. Walsh, 1982: On modeling seasonal and interannual fluctuations of Arctic sea ice. *J. Phys. Oceanogr.*, **12**, 1514–1523, https://doi.org/10.1175/1520-0485(1982)012<1514:OMSAIF>2.0.CO;2.

Hopkins, M. A., and A. S. Thorndike, 2006: Floe formation in Arctic sea ice. *J. Geophys. Res.*, **111**, C11S23, https://doi.org/10.1029/2005JC003352.

——, S. Frankenstein, and A. S. Thorndike, 2004: Formation of an aggregate scale in Arctic sea ice. *J. Geophys. Res.*, **109**, C01032, https://doi.org/10.1029/2003JC001855.

Hoteit, I., B. Cornuelle, A. Kohl, and D. Stammer, 2005: Treating strong adjoint sensitivities in tropical eddy-permitting variational data assimilation. *Quart. J. Roy. Meteor. Soc.*, **131**, 3659–3682, https://doi.org/10.1256/qj.05.97.

Houtekamer, P. L., and H. L. Mitchell, 1998: Data assimilation using an ensemble Kalman filter technique. *Mon. Wea. Rev.*, **126**, 796–811, https://doi.org/10.1175/1520-0493(1998)126<0796:DAUAEK.2.0.CO;2.

Hunke, E. C., and J. K. Dukowicz, 1997: An elastic–viscous–plastic model for sea ice dynamics. *J. Phys. Oceanogr.*, **27**, 1849–1867, https://doi.org/10.1175/1520-0485(1997)027<1849:AEVPMF>2.0.CO;2.

——, and W. H. Lipscomb, 2010: CICE: The Los Alamos Sea ice model—Documentation and software user's manual, version 4.1. Los Alamos National Laboratory Doc. LA-CC-06-012, 76 pp., http://csdms.colorado.edu/w/images/CICE_documentation_and_software_user's_manual.pdf.

Juricke, S., and T. Jung, 2014: Influence of stochastic sea ice parametrization on climate and the role of atmosphere–sea ice–ocean interaction. *Philos. Trans. Roy. Soc.*, **A372**, 20130283, https://doi.org/10.1098/rsta.2013.0283.

——, P. Lemke, R. Timmermann, and T. Rackow, 2013: Effects of stochastic ice strength perturbation on Arctic finite element sea ice modeling. *J. Climate*, **26**, 3785–3802, https://doi.org/10.1175/JCLI-D-12-00388.1.

Kauker, F., T. Kaminski, M. Karcher, R. Giering, R. Gerdes, and M. Voßbeck, 2009: Adjoint analysis of the 2007 all time Arctic sea-ice minimum. *Geophys. Res. Lett.*, **36**, L03707, https://doi.org/10.1029/2008GL036323.

Koldunov, N. V., and Coauthors, 2019: Fast EVP solutions in a high-resolution sea ice model. *J. Adv. Model. Earth Syst.*, **11**, 1269–1284, https://doi.org/10.1029/2018MS001485.

Komarov, A. S., and D. G. Barber, 2014: Sea ice motion tracking from sequential dual-polarization RADARSAT-2 images. *IEEE Trans. Geosci. Remote Sens.*, **52**, 121–136, https://doi.org/10.1109/TGRS.2012.2236845.

König Beatty, C., and D. M. Holland, 2010: Modeling landfast sea ice by adding tensile strength. *J. Phys. Oceanogr.*, **40**, 185–198, https://doi.org/10.1175/2009JPO4105.1.

Kreyscher, M., M. Harder, and P. Lemke, 1997: First results of the Sea-Ice Model Intercomparison Project (SIMIP). *Ann. Glaciol.*, **25**, 8–11, https://doi.org/10.3189/S0260305500013719.

——, ——, ——, and G. M. Flato, 2000: Results of the Sea Ice Model Intercomparison Project: Evaluation of sea ice rheology schemes for use in climate simulations. *J. Geophys. Res.*, **105**, 11 299–11 320, https://doi.org/10.1029/1999JC000016.

Laxon, S. W., and Coauthors, 2013: CryoSat-2 estimates of Arctic sea ice thickness and volume. *Geophys. Res. Lett.*, **40**, 732–737, https://doi.org/10.1002/grl.50193.

Le Dimet, F.-X., 1982: A general formalism of variational analysis. CIMMS Rep. 22, 34 pp.

——, and O. Talagrand, 1986: Variational algorithms for analysis and assimilation of meteorological observations: Theoretical aspects. *Tellus*, **38A**, 97–110, https://doi.org/10.1111/j.1600-0870.1986.tb00459.x.

Lemieux, J.-F., and F. Dupont, 2020: On the calculation of normalized viscous-plastic sea ice stress. *Geosci. Model Dev.*, **13**, 1763–1769, https://doi.org/10.5194/gmd-13-1763-2020.

——, B. Tremblay, S. Thomas, J. Sedláček, and L. A. Mysak, 2008: Using the preconditioned generalized minimum residual (GMRES) method to solve the sea-ice momentum equation. *J. Geophys. Res.*, **113**, C10004, https://doi.org/10.1029/2007JC004680.

——, D. A. Knoll, B. Tremblay, D. M. Holland, and M. Losch, 2012: A comparison of the Jacobian-free Newton–Krylov method and the EVP model for solving the sea ice momentum equation with a viscous-plastic formulation: A serial algorithm study. *J. Comput. Phys.*, **231**, 5926–5944, https://doi.org/10.1016/j.jcp.2012.05.024.

——, L. B. Tremblay, F. Dupont, M. Plante, G. C. Smith, and D. Dumont, 2015: A basal stress parameterization for modeling landfast ice. *J. Geophys. Res. Oceans*, **120**, 3157–3173, https://doi.org/10.1002/2014JC010678.

——, F. Dupont, P. Blain, F. Roy, G. C. Smith, and G. M. Flato, 2016: Improving the simulation of landfast ice by combining tensile strength and parameterization for grounded ridges. *J. Geophys. Res. Oceans*, **121**, 7354–7368, https://doi.org/10.1002/2016JC012006.

Lewis, J. M., and J. C. Derber, 1985: The use of adjoint equations to solve a variational adjustment problem with advective constraints. *Tellus*, **37A**, 309–322, https://doi.org/10.3402/tellusa.v37i4.11675.

Losch, M., A. Fuchs, J.-F. Lemieux, and A. Vanselow, 2014: A parallel Jacobian-free Newton–Krylov solver for a coupled sea ice ocean model. *J. Comput. Phys.*, **257**, 901–911, https://doi.org/10.1016/j.jcp.2013.09.026.

Massonnet, F., H. Goosse, T. Fichefet, and F. Counillon, 2014: Calibration of sea ice dynamic parameters in an ocean-sea ice model using an ensemble Kalman filter. *J. Geophys. Res. Oceans*, **119**, 4168–4184, https://doi.org/10.1002/2013JC009705.

Miller, P. A., S. W. Laxon, D. L. Feltham, and D. J. Cresswell, 2006: Optimization of a sea ice model using basinwide observations of Arctic sea ice thickness, extent, and velocity. *J. Climate*, **19**, 1089–1108, https://doi.org/10.1175/JCLI3648.1.

Nguyen, A. T., D. Menemenlis, and R. Kwok, 2011: Arctic ice-ocean simulation with optimized model parameters: Approach and assessment. *J. Geophys. Res.*, **116**, C04025, https://doi.org/10.1029/2010JC006573.

Nichols, N. K., 2003: Data assimilation: Aims and basic concepts. *Data Assimilation for the Earth System*, R. Swinbank, V. Shutyaev, and W. A. Lahoz, Eds., NATO Science Series, Vol. 26, Springer, 9–22.

——, 2010: Mathematical concepts of data assimilation. *Data Assimilation: Making Sense of Observations*, W. Lahoz, B. Khattatov, and R. Menard, Eds., Springer, 13–39.

Nitta, T., 1975: Some analyses of observing systems simulation experiments in relation to the First GARP Global Experiment. GARP Working Group on Numerical Experimentation Rep. 10, 35 pp.

Panteleev, G., M. Yaremchuk, J. N. Stroh, O. P. Francis, and R. Allard, 2020: Parameter optimization in sea ice models with elastic–viscoplastic rheology. *Cryosphere*, **14**, 4427–4451, https://doi.org/10.5194/tc-14-4427-2020.

Penenko, V. V., 1981: *Methods of Numerical Simulation of Atmospheric Processes*. Gidrometeoizdat, 350 pp.

Saad, Y., 2003: *Iterative Methods for Sparse Linear Systems*. SIAM, 520 pp., https://doi.org/10.1137/1.9780898718003.

Stroh, J. N., G. Panteleev, M. Yaremchuk, O. Francis, and R. Allard, 2019: Toward optimization of rheology in sea ice models through data assimilation. *J. Atmos. Oceanic Technol.*, **36**, 2365–2382, https://doi.org/10.1175/JTECH-D-18-0239.1.

Sumata, H., F. Kauker, M. Karcher, and R. Gerdes, 2019: Simultaneous parameter optimization of an Arctic sea ice–ocean model by a genetic algorithm. *Mon. Wea. Rev.*, **147**, 1899–1926, https://doi.org/10.1175/MWR-D-18-0360.1.

Tilling, R. L., A. Ridout, and A. Shepher, 2018: Estimating Arctic sea ice thickness and volume using CryoSat-2 radar altimeter data. *Adv. Space Res.*, **62**, 1203–1225, https://doi.org/10.1016/j.asr.2017.10.051.

Toyota, T., and N. Kimura, 2018: An examination of the sea ice rheology for seasonal ice zones based on ice drift and thickness observations. *J. Geophys. Res. Oceans*, **123**, 1406–1428, https://doi.org/10.1002/2017JC013627.

Tremblay, L.-B., and L. A. Mysak, 1997: Modeling sea ice as a granular material, including the dilatancy effect. *J. Phys. Oceanogr.*, **27**, 2342–2360, https://doi.org/10.1175/1520-0485(1997)027<2342:MSIAAG>2.0.CO;2.

——, and M. Hakakian, 2006: Estimating the sea ice compressive strength from satellite derived sea ice drift and NCEP reanalysis data. *J. Phys. Oceanogr.*, **36**, 2165–2172, https://doi.org/10.1175/JPO2954.1.

Ungermann, M., and M. Losch, 2018: An observationally based evaluation of subgrid scale ice thickness distributions simulated in a large-scale sea ice-ocean model of the Arctic Ocean. *J. Geophys. Res. Oceans*, **123**, 8052–8067, https://doi.org/10.1029/2018JC014022.

Uotila, P., S. O'Farrell, S. J. Marsland, and D. Bi, 2012: A sea-ice sensitivity study with a global ocean-ice model. *Ocean Modell.*, **51**, 1–18, https://doi.org/10.1016/j.ocemod.2012.04.002.

Vancoppenolle, M., T. Fichefet, H. Goosse, S. Bouillon, G. Madec, and M. A. M. Maqueda, 2009: Simulating the mass balance and salinity of Arctic and Antarctic sea ice. 1. Model description and validation. *Ocean Modell.*, **27**, 33–53, https://doi.org/10.1016/j.ocemod.2008.10.005.

Wunsch, C., 1996: *The Ocean Circulation Inverse Problem*. Cambridge University Press, 442 pp.

Zhang, J., and W. D. Hibler III, 1997: On an efficient numerical method for modeling sea ice dynamics. *J. Geophys. Res.*, **102**, 8691–8702, https://doi.org/10.1029/96JC03744.

——, and D. A. Rothrock, 2003: Modeling global sea ice with a thickness and enthalpy distribution model in generalized curvilinear coordinates. *Mon. Wea. Rev.*, **131**, 845–861, https://doi.org/10.1175/1520-0493(2003)131<0845:MGSIWA>2.0.CO;2.